Latent encoding of movement in primary visual cortex

Charlie Cosnier-Horeau[a,b,1], Hannah Germaine[a,b,1], Stephen Van Hooser[b,c], Isaiah Choi[a], Jérôme Ribot[d,2], and Jonathan D. Touboul[a,c,2,3]

Neurons in the primary visual cortex (V1) are classically thought to encode spatial features of visual stimuli through simple population codes: each neuron exhibits a preferred orientation and preferred spatial frequency that are invariant to other aspects of the visual stimulus. Here, we show that this simple rule does not apply to the representation of major features of stimulus motion, including stimulus direction and temporal frequency (TF). We collected an extensive dataset of cat V1 responses to stimuli covarying in orientation, direction, spatial frequency, and TF to assess the extent of motion selectivity. In over half of V1, we found that the preferred direction changed with stimulus TF, revealing four distinct map motifs embedded within V1's functional architecture. Additionally, preferred TF was mostly uniform across the cortical surface. Despite the lack of spatial modulation for the preferred TF map and the lack of invariance for the preferred direction map, we found using convolutional neural networks that direction, TF and stimulus speed can be accurately decoded from V1 responses at all cortical locations. These findings suggest that subtle modulations of V1 activity may convey fine information about stimulus motion, pointing to a novel primary sensory encoding mechanism despite complex co-variation of responses to multiple attributes across V1 neurons.

Perception of Movement | Primary Visual Cortex | Direction Map | Coding Accuracy

Significance Statement

Cortical maps are thought to be useful for efficient processing of sensory information. In the primary visual cortex (V1), they are believed to provide uniform coverage across the visual field, ensuring that all orientations, spatial frequencies, and other features are consistently represented at each location in visual space. This organization supports stable visual perception, but it remains unclear how V1 encodes motion, particularly speed. Here, we reveal that cat V1 represents motion speed in a distributed manner without spatially organized temporal frequency maps, and that direction maps vary with stimulus speed. Nonetheless, we show that information on speed and preferred direction is decodable at all cortical locations. These findings challenge the classical uniform coverage hypothesis for motion attributes, and suggest that V1 encodes motion information in a more flexible manner.

Motion perception, or the ability to infer the speed and direction of motion of elements in a visual scene, is a central capacity of the mammalian visual system essential for animal survival. It allows animals to navigate dynamic environments, avoid predators, and track prey. At a basic level, in such dynamic visual scenes, motion is characterized by local directions and velocities of points or edges in space. The neural mechanisms underlying motion perception have been a central topic of study in neuroscience (1), beginning with the pioneering work of Hubel and Wiesel (2), who identified direction-selective neurons in the primary visual cortex (V1) of cat. This discovery established V1 as a critical region for processing local motion signals, specifically direction, in addition to encoding other visual features such as orientation (2), spatial frequency (SF) (3), or position in the visual space. Motion selectivity has since been observed in V1 across various species, such as primates (4, 5), cats (6, 7), ferrets (8–11), and mice (12), underscoring a pivotal role of V1 in motion processing.

The processing of local motion components by V1 is then transmitted to higher visual areas, such as MT (V5) in Human or Macaque monkey, for further integration (10, 13–15). This pathway provides low-speed detection of objects in MT, while another pathway bypassing V1 brings information directly from the lateral geniculate nucleus for processing fast-moving stimuli (16, 17)]. Notably, neurons in MT in macaque are highly specialized for motion processing, responding robustly to moving stimuli to produce a coherent representation of complex motion patterns across the visual field. Moreover, these neurons are highly selective for speed (18–21), but do not cluster into functional columns with similar speed tuning (18).

This speed selectivity of MT neurons contrasts with V1, where experimental data present a more complex picture. For instance, in macaque V1, speed-tuned neurons are observed, particularly in complex cells (4, 5, 22). However, most neurons' temporal frequency selectivity is typically independent of SF. When tested with sine-wave gratings, many neurons indeed exhibit selectivity for temporal frequency (TF), which is the rate at which the grating drifts across the visual field, measured in cycles per second (Hz). As a result, many cells exhibit either a separable tuning for SF and TF, or a mixture between speed- and TF-selectivity, rather than pure speed tuning (5). Remarkably, despite this mixture of TF- and speed-selectivity, studies in human V1 have reported that SF and TF preferences cluster spatially in a binary manner (23). Specifically, some regions responded preferentially to low SF and high TF, while others responded preferentially to high SF and low TF. How

Author affiliations: [a]Department of Mathematics, Brandeis University, Waltham, MA 02446; [b]Department of Biology, Brandeis University, Waltham MA 02446; [c]Volen National Center for Complex Systems, Brandeis University; [d]Neuroglial Interactions in Cerebral Physiology and Pathologies, Center for Interdisciplinary Research in Biology, Collège de France, CNRS, INSERM, Labex Memolife, Université PSL, Paris, France

JDT and JR designed the research, the analytic tools, analyzed the data and wrote the paper. JR collected and processed the data. CCH and HG performed the analyses and wrote the paper. HG analyzed fracture displacement. IC ran machine learning codes to measure information processing. SVH designed the study and wrote the paper.

The authors declare no conflict of interest.

[1] CCH and HG contributed equally to this work.[2] JDT and JR contributed equally to this work.

[3]To whom correspondence should be addressed. E-mail: jtouboul@brandeis.edu

speed-tuned cells or those with mixed TF and speed selectivity, contribute to these maps remains elusive. Similar results have been found in mouse V1 (24), where cells also exhibit a continuum from speed to TF selectivity (12), as well as cat V1 (25). In sharp contrast, a study in promisian primates Bush Babies (*Otolemur garnetti*) found a uniform representation of TF, centered around 2 Hz, with no evidence of spatial organization (26). Altogether, these findings illustrate the complexity and variability of speed and TF representations in V1, with contrasting evidence from various species and no clear global consensus.

To further add complexity to the understanding of SF, TF, and speed tuning in V1, evidence from electrophysiological studies in cats (27) and ferrets (8) have suggested that while preferred orientation remains invariant to changes in TF, direction selectivity can vary significantly. In ferret V1, it has been shown that direction preference changes with TF, while orientation tuning remains stable across a range of temporal frequencies (8). Similarly, in the cat visual cortex, direction selectivity is strongest at low temporal frequencies (1–2 Hz) but diminishes or even reverses at higher temporal frequencies (27). These findings suggest that TF/speed maps and direction maps could co-vary and should thus be studied together to fully understand how motion is encoded in V1.

In this study, we studied speed selectivity in cat V1 (areas 17) using high-resolution intrinsic optical imaging. Leveraging recent advancements in stimulation techniques and analysis methods (28–30), we collected an extensive dataset of V1 responses to a variety of stimuli changing in orientation, direction, SF and TF. By combining unbiased computational analyses and targeted selectivity and topology inquiries, we examined how functional maps of orientation and direction varied across 45 combinations of SF and TF. Additionally, we explored V1's ability to decode speed, SF and TF using advanced imaging data decoding and statistical learning. These approaches have been applied not only to decode stimuli orientation (31, 32) and direction (33) in Human, but also to investigate their representation with working memory (34–36) and mental imagery (37–40) and even to classify functional efficiency of aging cortices (41). Moreover, these methods allow for a more detailed assessment of brain-activity patterns, revealing how even non-maximally responding regions contribute to decoding stimuli, as seen in previous studies (42). We show that spatially distributed V1 activity patterns contain fine local information about the direction and speed of motion. Additionally, while changes in TF left orientation maps unaltered, we found a significant remapping of the direction maps, with smooth variations of the position of the direction fractures, and constant movement speed of movement coincided with fracture immobility. Finally, we investigated topological changes across different speeds and classified these into four distinct topological motifs with varying contributions to speed decoding. This approach reveals how functional maps in V1 integrate motion-related attributes like TF and speed, providing novel insights into the neural encoding of complex motion dynamics.

Results

A. Uniform TF tuning and invariant orientation preference. We began our investigation by examining how changes in stimulus motion properties (direction and TF) affected raw activity in V1. For this purpose, we used a rotating and drifting sinusoidal grating (29, 30) to probe responses in cat V1 across all orientations and directions (discretized into 200 values), 9 temporal frequencies (ranging from 0.38 to 5.37 cycles per second) and 5 spatial frequencies (from 0.15 to 1.65 cycles per degree).

We observed that patterns of activity displayed different responses upon changes in stimulus properties (Figure 1). Because we are interested in stimuli eliciting maximal responses as well as in the spatial reorganization of activity upon changes in stimulus properties, we decompose the raw activity into two independent quantities: (i) the signal amplitude across the map for a given condition, and (ii) the normalized signal, which is an affine transformation of the raw signal bringing the values between 0 and 1. Although in nature firing rate amplitudes are function of a variety of properties of the stimulus (e.g., contrast and intensity) and attention mechanisms, it is classically considered that, within the controlled conditions of the experiment, changes in raw signal amplitude inform us of the features that elicit maximal firing rates overall. Normalized signals instead provide information about the spatial reorganization of activity upon changes in stimulus properties. Varying the stimulus direction (Figure 1A, top row) caused major modifications in the spatial organization of activity, as visible in the normalized maps but the signal intensity remained constant (right). In contrast, changes in TF elicited minimal changes in the spatial organization of activity, but the maximal intensity of the signal showed a clear dependence in TF, with a bell-shaped response curve peaked at 1.24 Hz (Figure 1B).

The resulting preferred TF map did not exhibit spatial organization, with a globally spatially uniform dependence in TF and a majority of cortical locations (90.0%) exhibiting maximal responses for TF in [1.24,2.00] Hz (Figure 1C, and also Supplementary Figures S1 and S2 for two other animals). This uniform preference is of the one found in Bush Baby (**?**), and stands in sharp contrast with the spatial organization of other visual attributes, such as orientation or SF, where each cortical location marks a clear preference that spans a wide range of stimulus conditions (2, 28, 43). Interestingly, variations in TF had no discernible effect on the representation of orientation (Figure 1D and Supplementary figures S3 and S4 for two other animals). This map remained strikingly invariant with stimulus TF as quantified by the low median absolute deviation in preferred orientation upon TF variation (averaged across all cortical locations, mad $= 0.04 \pm 0.02$, 0.05 ± 0.03, 0.03 ± 0.02 rad for the three animals, see Supplementary Figure 5). Altogether, this data argues for a uniform encoding of TF in V1 and no effect on preferred orientation.

Smooth Differential Responses encode TF in V1. Despite this apparent uniformity in TF representation, we explored whether changes in activity could convey information about stimulus TF. To infer the presence of information on TF that could possibly be accessible to areas downstream of V1, we trained a convolutional neural network (CNN) to evaluate stimulus direction and TF from raw or rescaled responses. We found that the CNN was able to accurately decode both direction and TF from V1 signals with high levels of accuracy(Figure 1E), both from the raw signals and from the normalized activity. The ability to decode the direction of motion from V1 activity is consistent with previous findings (33, 44, 45), and is expected, as strong activity shifts occur in response to changes in stimulus direction. However, given the low level of dependence of V1 response amplitudes on TF, particularly when rescaling maps of activity, it was unexpected to observe that TF could be accurately decoded from raw brain signals. This suggests that while the TF map is not organized into spatial patterns preferring various TFs, subtle differential patterns of activity across the cortical surface may still encode TF information in a manner accessible through advanced neural decoding methods.

To locate this information, we computed the difference between renormalized activity maps and a reference condition(Fig. 1F; see also Supplementary Figures S5 and S6 for a more exhaustive representation of a set of differential responses, as well as Supplementary Figure S7 estimating the norm of the difference between response maps for all three animals). This process uncovered a rich and smooth structure, with amplitude and spatial organization showing progressive variation upon changes in TF. This spatial organization revealed that, while the primary structure reflects a strong preference for direction, TF induces second-order fluctuations in the responses that could potentially carry information about the stimulus TF. To appreciate the emergence of these differential responses, we examined the response amplitudes at individual cortical locations for multiple directions and temporal frequencies (Figure 1G). Remarkably, we found that while most directions considered were associated with unimodal responses peaked around the common preferred TF, the precise dependence in TF of response amplitudes was distinct between different directions at the same location. In Figure 1G, we depicted responses at the preferred and opposite direction, as well as responses associated with a direction perpendicular to the preferred direction. All three curves showed vastly distinct profiles, which allows the emergence of complex differential structures all the while maintaining globally uniform preferences in TF and unchanged first-order responses. Furthermore, Figure 1G also confirmed, consistently with previous work (8, 27), that specific locations may change preferred direction according to TF (black triangles in Fig. 1G), an effect we explored in more detail in subsequent sections.

Altogether, these findings show that while we found that the preferred TF map is globally uniform, the minute changes in amplitude with stimulus TF differ from location to location, suggesting that V1 encodes more nuanced information about TF than previously recognized.

Continuous changes in direction maps fractures. We further explored the structure of changes in direction preference by reconstructing and analyzing preferred direction maps for each combination of temporal and spatial frequency tested. We observed substantial variations in direction maps upon variation of spatial and temporal frequency (Figure AA and Supplementary Figures S8A and S9A for the other two animals), with a mean absolute deviation tripled compared to that associated with orientation maps (0.12 + 0.11 rad, 0.17 + 0.13 rad, and 0.09 + 0.09 rad for the three animals). These variations in direction maps closely align with changes in direction tuning curves upon TF variation, as suggested by single-cell studies in ferret (8**?**) and exemplified for two cortical locations for different values of stimulus SF and TF (Red and blue curves, Figure AB). Moreover, the spatial location of these shift in preferred direction were not confined to the vicinity of pinwheel centers (Figure AC and Supplementary Figures S8B and S9B for the other two animals). Instead, large regions of the cortical surface switched their preferred direction (Cat 1: 80.23% , cat 2: 59.20%, cat 3: 77.00%), with no significant directional bias (Rao test for uniformity, corrected for continuity of the maps; see Methods).

The matrix layout of the different maps in Figure AA additionally suggests that changes in direction maps are not isotropic when stimulus SF or TF are varied independently. Instead, the changes seem dependent on specific combinations of the two stimulus properties. A physically relevant parameter combining SF and TF is the speed. Indeed, when considering the drifting gratings used as stimulus inputs, the speed, expressed as degree of visual angle per second, is defined as the ratio of TF to SF. This speed index is depicted as the greyscale background in Figure AA. To estimate the axes of maximal sensitivity in direction maps upon changes in SF and TF, we quantified the similarity of direction maps across all conditions. We found that maximal similarity between maps was achieved along a linear axis in the logarithmic scale of TF and SF differences. By fitting a multivariate Gaussian function over a range up to 4.6 octaves of SF and TF differences (i.e. $\frac{TF_1}{TF_2}$ and $\frac{SF_1}{SF_2} < 25$), we identified that the main axis of the fit followed the line $\log(TF) \approx 0.84 \log(SF)$ (or $\xi = 0.84$). This relationship reflects an intermediate scaling between pure speed and pure TF (cat 2, $\xi = 0.78$; cat 3, $\xi = 0.94$; see Supplementary Figure S10). Overall, our findings indicate that there are co-organized changes across the majority of the direction maps as TF and SF vary, following an axis between pure-TF and pure-speed tuning. This suggests that V1 direction maps integrate information from both TF and SF in a coordinated manner, tuned to a combination of speed and TF.

Fractures remain stable for constant stimulus speed. Modulo π, direction preference maps share the typical organization of orientation preference maps, which are continuous except at orientation pinwheels - punctual singularities around which all orientations are represented. Due to this constraint, direction maps are bound to display linear singularities, called fractures, where direction preference displays a sharp discontinuity, shifting to the opposite preferred direction (Figure 3A). Topologically, each pinwheel is associated with at least one fracture. Typically, direction fractures consist of linear singularities connecting two pinwheels or forming closed loops.

To investigate changes in direction preference and potential topological changes in direction maps, we meticulously tracked

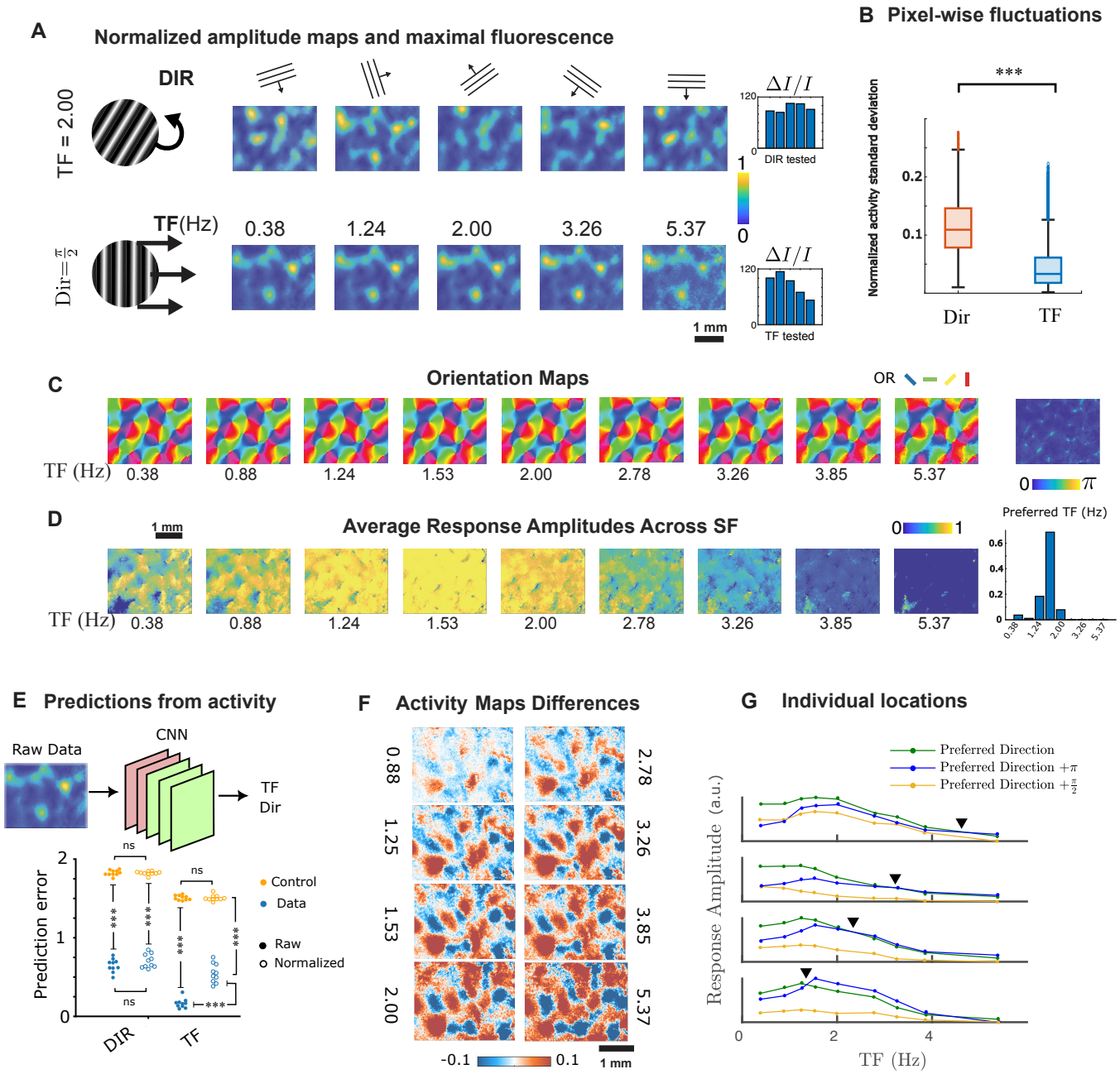

Fig. 1. Uniform representation of temporal frequency preference with decodable information. A-D: Invariant features. A. Top: Response amplitude for various directions of motion and a fixed TF (2 Hz). Bottom: Response amplitude for various TFs and a fixed direction (righward, $\pi/2$) (bottom). In both panels, the stimulus spatial frequency is 0.29 cycles/degree. The responses are normalized between 0 and 1. The mean response amplitude for each stimulus condition is plotted on the right. B. Fluctuations of the response magnitude at each pixel when varying stimulus direction and stimulus TF. Median standard deviation for direction is 0.11 ± 0.04 mad, while for TF it is 0.03 ± 0.03 mad (two-sample t-test $p < 0.001$). C. Amplitude of responses to changes in TF, averaged across SF at preferred orientation. The preferred TF shows a unimodal distribution (histogram on the right) that peaks at 1.53 Hz, with 90% of locations within the 1.24-2.00 Hz range (cat 2: 81% and cat 3: 78%). D. Orientation maps are largely invariant to changes in stimulus TF (median standard deviation of 0.2 ± 0.15 mad radian), with higher fluctuations apparently concentrated near orientation pinwheel centers . E. Top: The architecture of the Convolutional Neural Network (CNN) is composed of five layers (two convolutional in pink and three rectified linear layers in green). This CNN was trained to predict stimulus TF and direction from V1 responses. Bottom: Prediction error (blue dots) shows high predictability for TF and direction compared to controls (same dataset but where TF and Direction were randomly shuffled, yellow dots) (10-fold cross-validation, two-sample t-test $p < 0.001$). F. Difference between V1 response maps between $TF = 0.38$ and other stimulus TFs. These differences show a gradual increase in strength with increasing TFs, as well as smooth variations in spatial organization. Stimulus spatial frequency is $SF = 0.29$ cycles/degree and stimulus direction $\pi/2$. G. Response tuning curves of four cortical locations separated by $87\mu m$ along a line, showing changes in response with varying stimulus TF. The preferred direction was determined at TF=0.38 Hz, and response tuning curves are displayed for the preferred direction (green), the opposite direction (blue) and the orthogonal direction (orange). Black triangles indicate switches in preferred direction for each cortical location.

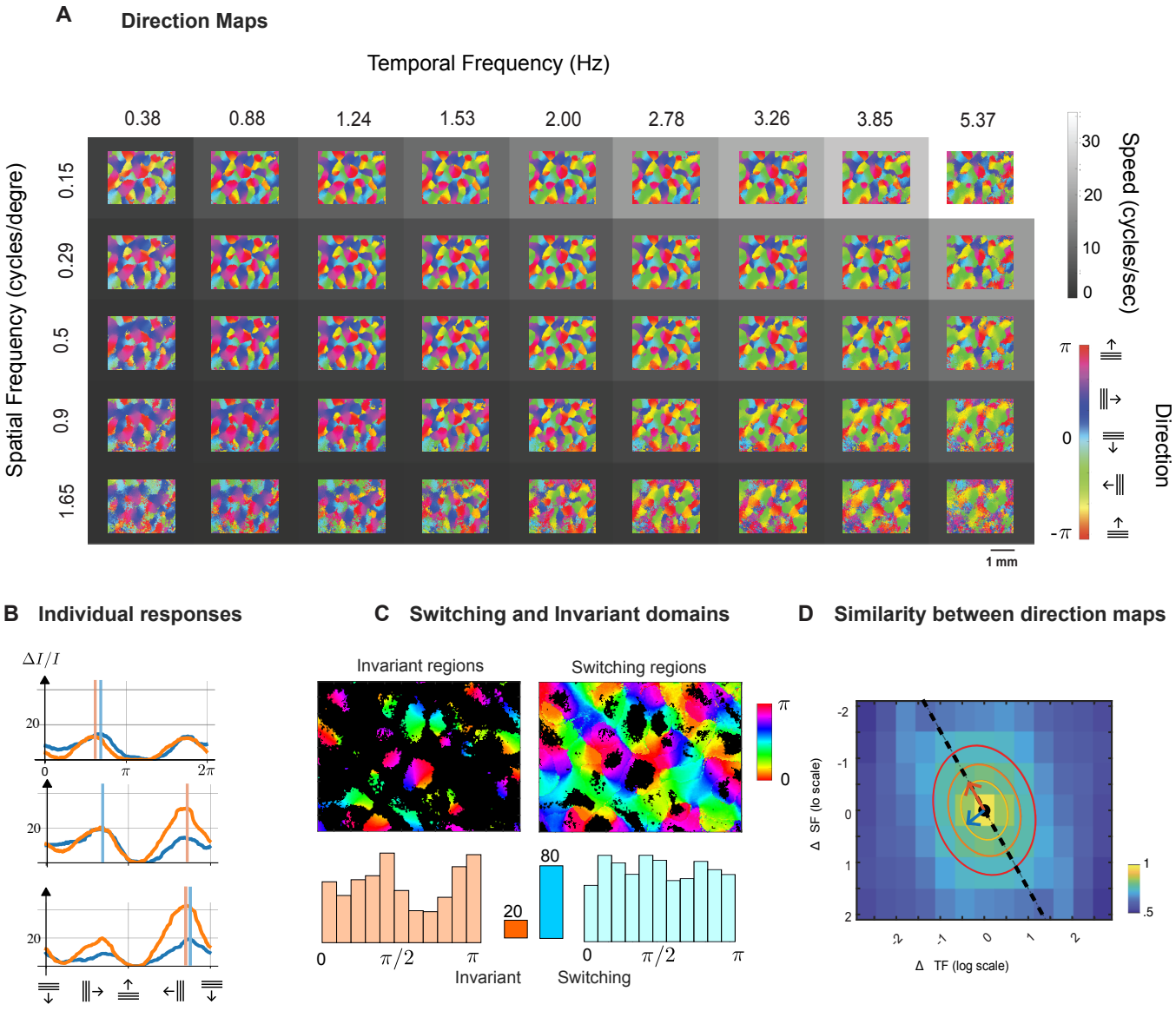

Fig. 2. Non-invariance of direction preference representation with stimulus temporal frequency and speed. A. Direction preference maps for all combinations of stimulus spatial frequency and TF,overlaid on a grey scale grid indicating stimulus speed. B Illustration of the direction tuning curves for two different cortical locations (blue and orange curves) and three different conditions. Vertical bars indicate the preferred direction of each tuning curve. C. Representation of cortical locations that do not switch direction preference (left, 19.97% of the cortical area) and those that do switch direction preference (right, 80.03% of the cortical area) overlaid on the invariant preferred orientation map. The distributions of preferred orientation are shown below, and exhibit no difference when corrected for continuity $p > 0.1$, see test in Methods). D. Similarity index between pairs of direction maps, plotted according to the logarithmic distance between stimulus TF and spatial frequency. The axis of anisotropy is estimated using a multivariate Gaussian fit, with ellipses representing two level sets of the fitted Gaussian. The main axis is shown as a black dashed line, with a fit of $\log\left(\frac{TF}{TF_0}\right) \approx 0.84 \log\left(\frac{SF}{SF_0}\right)$. The minor axis is indicated by a blue vector.

direction fractures in each of the 45 direction maps (Fig. 3C and Supplementary Figures S8C and S9C for the other two animals). These fractures exhibited continuous variations in response to changes in speed, covering large regions of the cortical map. To quantify changes in fracture positions, we computed the cumulative distance between fractures (see Methods) as a function of stimulus conditions. Similarly to the observations in Figure AD, when plotted against the logarithmic SF and TF differences (Figure AB), we observed that the greatest invariance occurred along a slanted axis as expected from our results in Figure AD. This invariance became even more apparent when fractures were grouped according to speed: positions of fractures showed only minor variations for stimuli associated with similar speeds, even when SF and TF differed significantly (Figure 3D).

As the stimulus speed changed, some fractures remained spatially stable (Figure 3E1), while some others were gradually shifting, in a majority of cases moving along a given axis maintaining the identity of the pinwheels they are connected to (Figure 3E2). Occasionally, fractures formed detached closed loops (bubbling, Figure 3E3), or exchanged which pinwheel they were connected to (saddles, Figure 3E4). Of note, similar instances were found in all animals considered (see Supplementary Figures S8C and S9C). These topological changes actually arise from the continuous morphing of the fracture shapes, as illustrated in the three dimensional reconstructions of the fracture surfaces, where speed is represented as altitude.

Altogether, these findings reveal that direction fractures in V1 are globally stable for stimuli with similar speeds. Yet, the changes in stimulus speed also lead to dynamic topological modifications in fracture patterns.

Local decoding of speed from V1 activity . The observation that direction maps are not unique, but vary with speed, puts into question the possibility of decoding the direction of stimuli with distinct speeds, but also the decoding of speed and direction independently. To explore this, we used a similar convolutional neural network as in Fig. 1E) and trained a regression algorithm to predict speed from raw or renormalized data (Figure 4A). Remarkably, we found that raw (Figure 4B) or normalized (Figure 4C) brain activity images produced highly accurate speed and direction predictions, with performance significantly better than control datasets where the association between brain activity images and speed was randomized. Furthermore, we found that speed and direction information can be decoded locally, in cortical regions as small as $123x123\mu m^2$ (10-by-10 pixels with our resolution) (Figure 4C). Even in these small regions, the decoding accuracies were comparable to that of larger areas, suggesting that speed encoding is a local property of V1 responses. This may imply the animal's capacity to detect complex movements associated with various speeds and directions at different locations in the visual scene.

Finding that speed was decodable at local scales thus allowed the investigation of potential correlations between cortical position in V1 and speed coding accuracy. To do that, we computed on a fine grid of non-overlapping regions of $123x123\mu m^2$, speed and direction decoding accuracy over a large area of V1 (Figure 4D, left panels, top for speed and bottom for direction). While there were some spatial fluctuations in accuracy, no clear correlation emerged between these spatial fluctuations and changes in preferred direction with stimulus speed. To quantify this observation, we labeled each window as either "switching" or "stable" depending on whether the majority of pixels contained in that area changed direction preference with speed. Notably, we found no significant difference in decoding accuracy between these two regions (Figure 4D, right panels). This suggests that the spatial variations in direction preference and speed decoding accuracy are two sides of the same coin, the differential changes in response amplitudes rather than consequences of one another. Also, no correlations were found between the coding accuracies in speed and direction.

Discussion

Our findings provide new insights into how motion attributes are represented in V1 and their potential implications for visual perception. We demonstrated that TF preference is uniformly distributed across V1, lacking spatial modulation typical of other visual attributes. Moreover, direction preference exhibits significant remapping in response to changes in TF and speed, with about 60-80% of the cortical area switching preferred direction under varying conditions, putting in perspective the notion of a well-defined direction map in V1, but revealing a collection of maps smoothly varying upon changes in TF. In sharp contrast, the OR map was invariant to changes in TF, revealing that some maps are robust to changes in a given attribute while others are non-invariant. Despite these non-invariant direction maps and uniform TF representation, the changes in cortical activity associated can provide fine and local information about the stimulus, as we showed using convolutional neural networks (CNNs) to decode motion attributes from brain signals, including TF, speed, and direction. These results formally establish that maps organized according to stimulus preferences covering the range of percepts, or even representations of visual attributes that are invariant upon changes in other stimulus properties, are not necessary for visual perception. This offers a novel perspective on how V1 may encode motion attributes.

Pioneering investigations of TF representation in cat V1 have reported the presence of binary domains with a co-representation of SF: regions responding preferentially to low SF and high TF or high SF and low TF (25). While subsequent studies have revealed that SF representation in cat V1 spans a broad range of preferences and is predominantly continuous (28, 43), the case of TF representation has not been reexamined. Here, we demonstrate that TF preference in V1 is mostly uniform across the cortical surface, with a 80-90% of cortical locations exhibiting maximal responses in the 1.24-2 Hz range, and lacking the spatial modulation suggested by earlier studies. These findings align closely with results obtained in promisian primates Bush Babies (**?**), where TF preference was similarly reported to be uniformly distributed, centered around 2 Hz. Additionally, TF had a significant impact on the representation of direction preference. An organization for direction preference in cat V1 has been reported (9, 46**?**), but these studies examined responses to a single TF of stimulation. Our data reveal that direction map is not invariant with respect to stimulus TF and that TF and direction should be studied together. Interestingly, these shifts in direction preference with stimulus TF align with specific map motifs, suggesting an underlying structure to this variability.

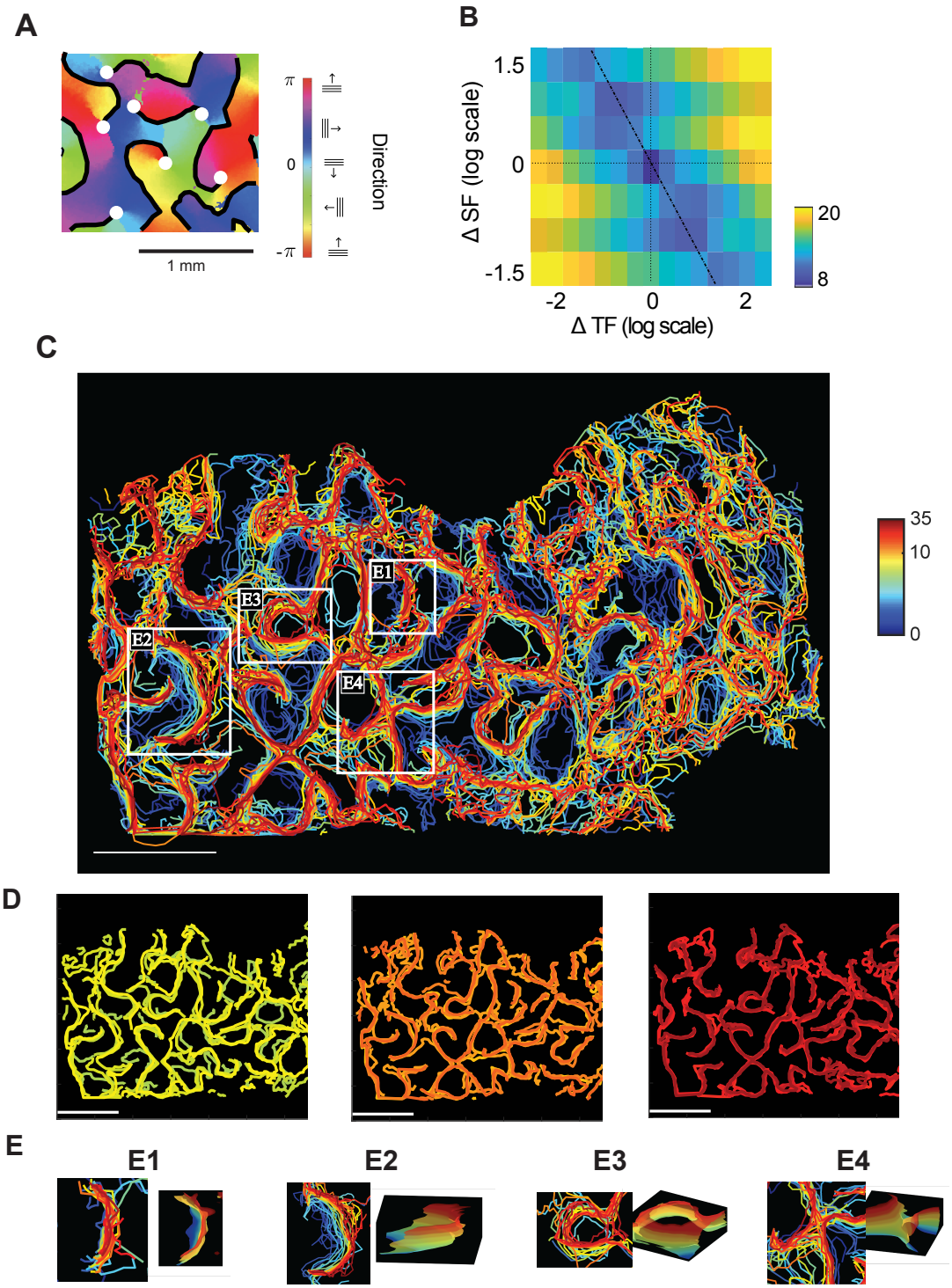

Fig. 3. Shifts in direction maps fractures with speed reveal stereotyped motifs A. Illustration of preferred direction map fractures (black contours) overlaid with orientation pinwheel centers (white dots) for $TF = 1.53$ Hz and SF=0.29 cpd. B. Average distance between fractures in pairs of direction maps, plotted according to the logarithmic difference between stimulus TF and spatial frequency. Minimal changes occur along a slanted axis (dotted line). C. Direction fractures computed for each combination of stimulus TF and spatial frequency, colored-coded according to speed (in logarithmic scale). D. Representation of direction fractures across different speed intervals, where minimal changes occur as shown in B: left panel shows speeds in $[2.45, 5.5]$ degree/second (7 conditions), middle panels in $v \in [6, 14]$ degree/second (7 conditions), and right panel in $v \in [14, 33]$ degree/second (5 conditions). E. Illustration of typical fracture movements with speed, shown as a zoomed-in view from C with a 3D surface representation where the (x, y)-axes represent the cortical surface and $(z$-axis) represents speed. E1: Invariant direction fractures. E2: Traveling fractures, where fractures shift in one direction with speed. E3: Bubbling fractures, where one fracture splits into two, with one forming a closed loop. E4: Crossings fractures, where two fractures exchange their connections.

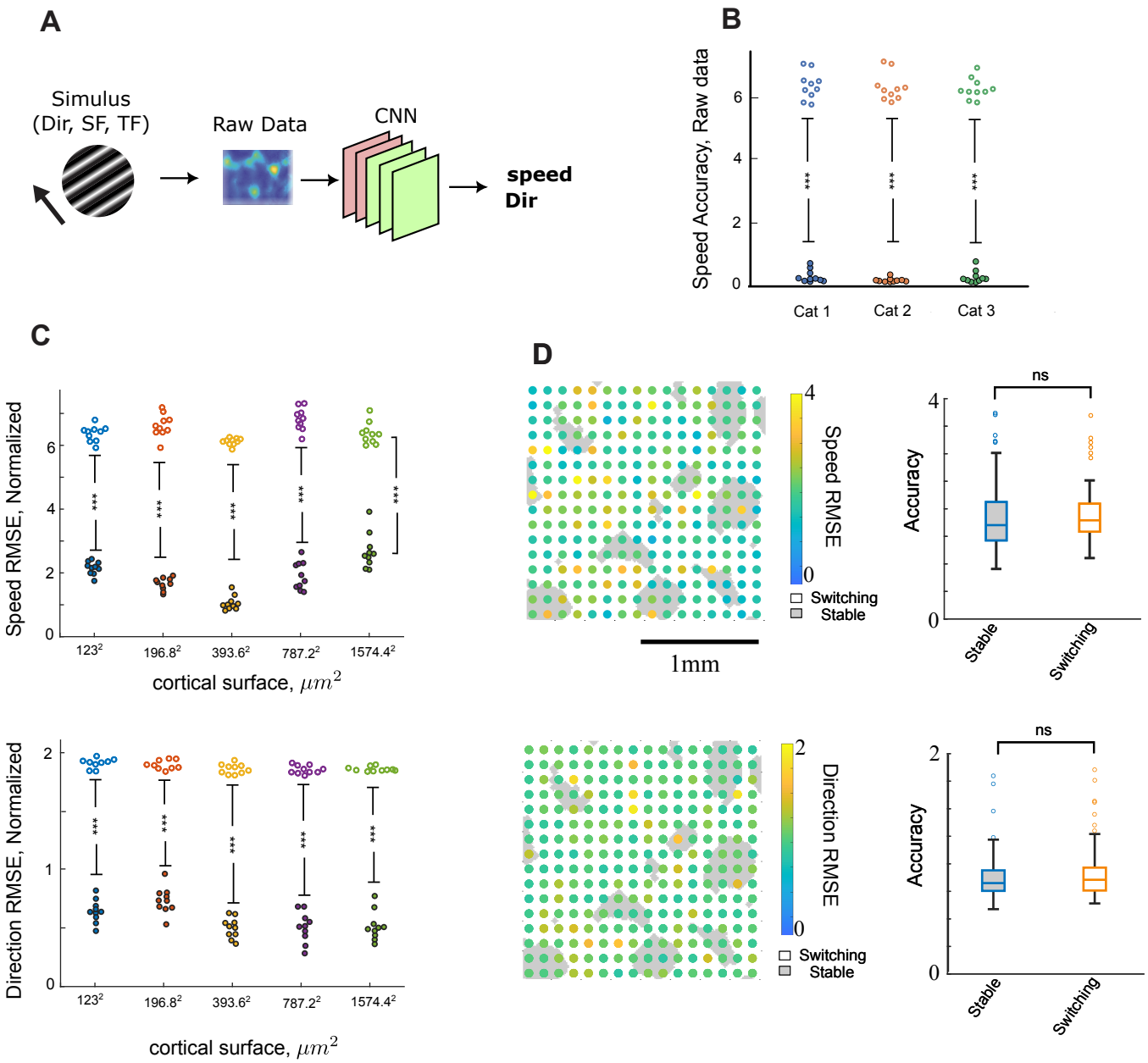

Fig. 4. Preferred direction and preferred speed are accurately decoded from local V1 responses despite uniform or non-invariant representation A. Illustration of the convolutional neural network architecture. It is composed of five layers: two convolutional layers (pink) and three linear layers (green), with rectified linear activation functions. B. Prediction error for speed accuracy across three animals shows high predictability compared to controls (same dataset but where TF and Direction were randomly shuffled) (10-fold cross-validation, two-sample t-test $p < 0.001$). C. Prediction error for speed accuracy (top) and direction accuracy (bottom) across cortical regions with different size (from $123 \times 123 \mu m^2$ to $1574.4 \times 1574.4 \mu m^2$), shows high predicability compared to controls (same dataset but where TF and Direction were randomly shuffled) (10-fold cross-validation, two-sample t-test $p < 0.001$). D. Spatial organization of coding accuracy for preferred speed (top) and preferred direction (bottom) of non-overlapping cortical windows with 10×10 pixels ($123 \times 123 \mu m^2$, colored circles) overlaid with invariant (grey) and non-invariant (white) direction domains. Right panels show no significant difference in coding accuracy between invariant and non-invariant direction domains (2-sample t-test $p > 0.1$).

Our results also shed new light on the uniform coverage hypothesis, a foundational principle of cortical organization. The uniform coverage principle postulates that all possible values of a visual attribute are evenly represented across the cortical surface (47), into parallel maps that can encode many combinations of attributes. In V1, this principle has been associated with the orthogonal arrangement of invariant functional maps, such as those for orientation, spatial frequency, and eye dominance, to optimize coverage of stimulus space (48–50). Our findings challenge the uniform coverage hypothesis for motion-related features in several ways. First, the predominantly uniform distribution of TF preference in cat V1 within the 1.24–2 Hz range limits access to other TF values, contradicting the expectation of even representation across the attribute's full range. Second, the dynamic shifts in direction preference with stimulus TF violate the principle of invariant representation. These observations suggest that uniform coverage may not extend to motion-related features and that alternative mechanisms might govern their cortical representation.

Our CNN analysis provides compelling evidence that functional maps in cat V1 are not be necessary for the perception of motion attributes. Indeed, despite the lack of a structured TF map and the non-invariance of direction maps, we demonstrated that TF, speed, and direction information could be accurately decoded from local V1 responses at any cortical location. Notably, no differences in decoding accuracy were found between zones with invariant direction preference and those with switching direction preference. The question of the functional significance of maps for visual perception echoes findings in squirrel monkeys, where, variability in the expression of ocular dominance columns -from well-developed to nearly absent- does not impair binocular vision (51, 52), challenging the presumed necessity of these maps for stereopsis. Similarly, in rodents (7, 53), lagomorphs (54) and grey squirrels (55), robust visual processing occurs without the columnar organization of orientation or direction, underscoring that maps are not indispensable for perception. Instead, we suggest that distributed activity patterns in V1 may convey rich information about motion attributes.

How, developmentally, these co-representations arise remain a central question. Mathematical or computational models, having the ability to successfully reproduce different aspects of V1 response properties (56–62) (see (63) for a comparison of models on orientation tuning), may altogether suggest that plasticity and the nature of visual stimuli subtend map organizations. In particular, models based on the statistics of natural images and their processing (64–68) or neurogeometric models (69–71) tend to suggest that geometric structures and the nature of stimuli are the source of functional architectures. An intriguing avenue of research would be to explore these models for speed invariance, fractures or the underlying structural details and timescales of integration. Some of our topological observations and rules of change arise naturally from biological constraints, such as the co-organization of orientation and direction tuning, and stability of orientation tuning across TF changes. The only direction map changes can be due to single cells' preference modulation by π, and the structure of connectivity in V1 helps ensure mostly smooth preference changes across cortex. Testing if models of V1 and visual perception generate similar responses to varying TF and speeds offer an interesting perspective of this work.

The combination of beautiful and rule-bound topological changes with the co-organization of response properties to all four stimulus properties (OR, DIR, TF, SF), naturally leads to developmental and structural questions. Developmentally, we know that direction selectivity requires visual experience in carnivores(72, 73) and primates(**? ?**), so it is of interest whether co-organization with speed tuning, in particular, follows a strict developmental ordering or is influenced by experience. Further, direction maps and orientation maps are co-organized spatially in columns about pinwheel centers, and given the finding that direction maps change with TF /speed and orientation maps remain constant a natural question arises of whether there is a hierarchy of priority and stability in V1 feature processing, with a strong robustness of orientation tuning invariance, and whether this stability coincides with bottom-up versus top-down activity modulation. The prior segregation of motion processing to higher-order regions, and stationary processing to V1 followed a bottom-up theory of building complexity in processing, but the recurrent connections from these "higher-order regions" in visual processing back to V1 calls into question the extent of the observed motion information arising as a consequence of "top-down" information transfer (11). One approach to addressing this question is investigating direction map changes under conditions of targeted optogenetic/chemogenetic silencing of projections to V1 from regions downstream.

Material and Methods

Surgical procedure

All experiments were performed in accordance with the relevant French guidelines and regulations. Intrinsic optical imaging was applied on young adult cats of either sex in good health and with no apparent malformations or pathologies. Animals were anesthetized with saffan (initial dose, 1.2 mg/kg, i.m.; supplements, 1:1 in saline, administered intravenously as needed). Following tracheal and venous cannulation, electrocardiogram, temperature, and expired CO2 probes were placed for continuous monitoring and animals were secured in the Horsley-Clarke stereotactic frame in preparation for acute recordings. The scalp was incised in the sagittal plane, and a large craniotomy was performed over area 17. The nictitating membranes were then retracted with eye drops (Neo-Synephrine 5%, Ciba Vision Ophthalmics), and the pupils were dilated with atropine eye drops (atropine 1%, MSD-Chibret). Scleral lenses were placed to protect the cornea and focus the eyes on the tangent screen 28.5 cm away. Animals were then paralyzed with an infusion of Pavulon (0.2 mL/kg (0.4 mg/kg), i.v.), and breathing was assisted artificially through a tracheal cannula with a 3:2 mixture of N2O and O2 containing 0.5-1.0% isoflurane. The respiration frequency was adjusted to 18 breaths/minute, and the volume adapted to the ratio of exhaled CO2 (partial pressure of carbon dioxide at 4%). Paralysis was maintained throughout the recording by continuous infusion of a mixture of Pavulon (0.1 mL/kg/h) diluted in glucose (5%) and NaCl (0.9g/L). Following the recording session, animals were sacrificed using a lethal dose of pentobarbital.

Optical imaging

The cortex was illuminated at 545 nm to reveal the vascular pattern of the cortical surface, and at 700 nm to record the intrinsic signals. The focal plane was adjusted to 500 µm below the cortical surface. The optic discs were plotted by tapetal reflection on a sheet of paper covering the tangent screen placed 28.5 cm in front of the animal. The center of the screen was situated 8 cm below the middle of the two optic discs. Intrinsic optical signals were recorded while the animals were exposed to visual stimuli displayed on a CRT monitor subtending a visual angle of around 750x560. Frames were acquired by CCD video camera (1M60, DALSA) at the rate of 40 frames per second and were stored after binning by 2x2 pixels spatially and by 12 frames temporally using the LongDaq system (Optical Imaging). Images were acquired with a resolution of 12.3 μm/pixel.

Stimulation

Full-screen visual stimuli were presented continuously to the animal. Each stimulus consisted of sine-wave gratings drifting in one direction and rotating in a counter-clockwise manner [cite 54]. The angular speed of rotation was 2 cycles per minute. The contrast was set at 50% to ensure the production of smooth sine wave gratings [cite 55]. Nine temporal frequencies ranging in a logarithmic scale from 0.38 to 5.87 Hz, and 5 spatial frequencies ranging in a logarithmic scale from 0.15 to 1.65 cycles/degree were presented in random order. Ten full rotations were presented for each pair of temporal and spatial frequencies.

Image processing

Data analysis was based on the method developed by Kalatsky and Stryker (29, 30) to extract periodic signals from intrinsic data using Fourier series theory. First, data were pre-processed to remove slow-varying components using a multi-variate analysis technique called the generalized indicator function method (74, 75). Next, hemodynamic delays and magnitude attenuations induced by filtering properties of the hemodynamic signals were rectified by applying an inverse first-order low-pass filter with a 5 second time constant (29). A low-pass spatial filter (with a Gaussian kernel of 5x5 pixels and of 2 pixel standard deviation) was also applied for smoothing the data. A 3D median kernel was then applied in the direction of movement (about 25 degrees), temporal frequency (neighboring), and spatial frequency (neighboring) for smoothing of the extracted responses. Orientation and direction maps were then extracted by calculating Fourier coefficients for the first two modes along the angular component of the response for each pixel and each spatial and temporal frequency pair separately (30). The phase of the first Fourier mode was used to determine orientation preference, and the sum of the first two nodes allowed us to obtain the preferred and secondary directions of motion.

The similarity index between two direction maps used in Figure AD was estimated as follows. Consider two direction maps $\theta_1(x,y)$ and $\theta_2(x,y)$, where (x,y) are the coordinates on the cortex and that are associated to the same orientation map (that is, $\theta_1(x,y) - \theta_2(x,y) = 0 \mathrm{mod} \pi$, is defined by the average number of pixels whose preferred direction differ by more than $\pi/2$:

$$1 - \langle \mathbb{1}_{(} |\theta_1(x,y) - \theta_2(x,y)| \geq \pi/2) \rangle_{(x,y)\in \mathrm{cortex}}$$

where $\langle \cdot \rangle_{(x,y)\in \mathrm{cortex}}$ denotes the average on all points of the cortical map, and $\mathbb{1}_{condition}$ denotes the indicator function, equal to 1 when condition is satisfied and 0 otherwise. The choices of an indicator function and of a threshold $\pi/2$ are used to emphasize changes in the map that do not depend sensitively on the threshold. A test using the natural distance, $\langle |\theta_1(x) - \theta_2(x)| \rangle_{x\in \mathrm{cortex}}$, provides similar qualitative results.

Fracture Detection. To identify these fractures, we used an automatic extraction, identifying the maximal gradient in direction within a single map across x and y coordinates. As shown in Figure 3A, fractures tend to start and end at orientation pinwheel centers, which topographically makes sense given the co-organization of orientation and direction preference maps. Given the changes seen in direction maps in Figure 2, we proceeded to quantify the difference in fractures as a function of changing TF and SF in order to compare the axis of change.

Convolutional Neural Network. All Convolutional Neural Networks were implemented in Python 3 using PyTorch 1.12.1. Unless specified otherwise, they were trained on cropped images of size 256x256 pixels (i.e., $3.23 \times 3.23 \mu m^2$, for computational efficiency. All neural networks used shared the same architecture, composed of the following layers:

- 6 convolution layers with input images of size $N \times N$ pixels, single-channel with $N = 256$ unless specified otherwise. The size of the convolutional kernels is 5 pixels ($63\mu m$) - `Conv2d(1, 6, 5)`. The results were rectified using RELU functions.
- 6 max-pooling layers with kernel size 2×2, yielding 6 output images of size $N/2 \times N/2$
- 16 convolutional layer with input from all 6 maxpooling layers, with kernel size 5×5 and RELU rectification. These were then serving as an input to a regression algorithm composed of:
- a linear layer with input $16 * n^2$ with $n = N/4 - 3$ (typically, $n = 61$) and output 120, followed by RELU rectification,
- a linear layer with input size 120 and output 84, followed by RELU rectification, and, eventually
- the ouput layer, as a a linear layer with input size 84 and output size 1.

Loss was considered to be mean squared error, made periodic when predicting direction. The optimizer was Adams, learning rate 0.001 by default (0.0005 for windows smaller than 20×20 pixels, or $255.2 \times 255.2 \mu m^2$). All results reported here are associated with such a regression algorithm. Classification for TF (where the output is a tensor of size 9 instead of 1 and loss is a traditional categorical classification accuracy associated with the percentage of accurate classification) yielded similar results. For smaller windows of size less than 20×20 pixels, we replaced the size of convolutional kernels by smaller kernels of size 3×3 pixels. Batch sizes were set to 32, and the number of epochs was set to 200, although convergence happened after around 100 epoch or less depending on the window size.

We used 10-fold cross-validation to generate our results. Controls were generated by using identical processes but shuffling the labels to be learned. Comparisons between the dataset and the controls were done using two-sample t-test.

ACKNOWLEDGMENTS. JDT acknowledges partial support from National Institute of Health R01GM152811, National Science Foundation, Division of Mathematical Sciences 1951369, and Swartz Foundation for a fellowship partially supporting CCH over the course of the project. SVH acknowledges support from NIH R01EY022122.

1. TD Albright, GR Stoner, Visual motion perception. *Proc. Natl. Acad. Sci.* **92**, 2433–2440 (1995).
2. DH Hubel, TN Wiesel, Receptive fields, binocular interaction and functional architecture in the cat's visual cortex. *The J. physiology* **160**, 106–154 (1962).
3. L Maffei, A Fiorentini, The visual cortex as a spatial frequency analyser. *Vis. research* **13**, 1255–1267 (1973).
4. G Orban, H Kennedy, J Bullier, Velocity sensitivity and direction selectivity of neurons in areas v1 and v2 of the monkey: influence of eccentricity. *J. neurophysiology* **56**, 462–480 (1986).
5. NJ Priebe, SG Lisberger, JA Movshon, Tuning for spatiotemporal frequency and speed in directionally selective neurons of macaque striate cortex. *J. Neurosci.* **26**, 2941–2950 (2006).
6. CD Gilbert, Laminar differences in receptive field properties of cells in cat primary visual cortex. *The J. physiology* **268**, 391–421 (1977).
7. K Ohki, S Chung, YH Ch'ng, P Kara, RC Reid, Functional imaging with cellular resolution reveals precise micro-architecture in visual cortex. *Nature* **433**, 597–603 (2005).
8. BD Moore IV, HJ Alitto, WM Usrey, Orientation tuning, but not direction selectivity, is invariant to temporal frequency in primary visual cortex. *J. neurophysiology* **94**, 1336–1345 (2005).
9. M Weliky, WH Bosking, D Fitzpatrick, A systematic map of direction preference in primary visual cortex. *Nature* **379**, 725–728 (1996).
10. AA Lempel, KJ Nielsen, Ferrets as a model for higher-level visual motion processing. *Curr. Biol.* **29**, 179–191 (2019).
11. AA Lempel, KJ Nielsen, Development of visual motion integration involves coordination of multiple cortical stages. *Elife* **10**, e59798 (2021).
12. ML Andermann, AM Kerlin, DK Roumis, LL Glickfeld, RC Reid, Functional specialization of mouse higher visual cortical areas. *Neuron* **72**, 1025–1039 (2011).
13. R Dubner, S Zeki, Response properties and receptive fields of cells in an anatomically defined region of the superior temporal sulcus in the monkey. *Brain research* (1971).
14. RT Born, DC Bradley, Structure and function of visual area mt. *Annu. Rev. Neurosci.* **28**, 157–189 (2005).
15. S Zeki, Area v5 – a microcosm of the visual brain. *Front. integrative neuroscience* **9**, 21 (2015).
16. J Zihl, D Von Cramon, N Mai, C Schmid, Disturbance of movement vision after bilateral posterior brain damage: further evidence and follow up observations. *Brain* **114**, 2235–2252 (1991).
17. S Shipp, Bd Jong, J Zihl, R Frackowiak, S Zeki, The brain activity related to residual motion vision in a patient with bilateral lesions of v5. *Brain* **117**, 1023–1038 (1994).
18. J Liu, WT Newsome, Functional organization of speed tuned neurons in visual area mt. *J. neurophysiology* **89**, 246–256 (2003).
19. L Lagae, S Raiguel, G Orban, Speed and direction selectivity of macaque middle temporal neurons. *J. neurophysiology* **69**, 19–39 (1993).
20. JH Maunsell, DC Van Essen, Functional properties of neurons in middle temporal visual area of the macaque monkey. i. selectivity for stimulus direction, speed, and orientation. *J. neurophysiology* **49**, 1127–1147 (1983).
21. JA Perrone, A Thiele, Speed skills: measuring the visual speed analyzing properties of primate mt neurons. *Nat. neuroscience* **4**, 526–532 (2001).
22. K Foster, JP Gaska, M Nagler, D Pollen, Spatial and temporal frequency selectivity of neurones in visual cortical areas v1 and v2 of the macaque monkey. *The J. physiology* **365**, 331–363 (1985).
23. P Sun, et al., A temporal frequency–dependent functional architecture in human v1 revealed by high-resolution fmri. *Nat. neuroscience* **10**, 1404–1406 (2007).
24. W Ji, et al., Modularity in the organization of mouse primary visual cortex. *Neuron* **87**, 632–643 (2015).
25. D Shoham, M Hübener, S Schulze, A Grinvald, T Bonhoeffer, Spatio–temporal frequency domains and their relation to cytochrome oxidase staining in cat visual cortex. *Nature* **385**, 529–533 (1997).
26. I Khaytin, et al., Functional organization of temporal frequency selectivity in primate visual cortex. *Cereb. Cortex* **18**, 1828–1842 (2007).
27. AB Saul, AL Humphrey, Temporal-frequency tuning of direction selectivity in cat visual cortex. *Vis. neuroscience* **8**, 365–372 (1992).
28. J Ribot, Y Aushana, E Bui-Quoc, C Milleret, Organization and origin of spatial frequency maps in cat visual cortex. *J. Neurosci.* **33**, 13326–13343 (2013).
29. A Sauvage, G Hubert, J Touboul, J Ribot, The hemodynamic signal as a first-order low-pass temporal filter: Evidence and implications for neuroimaging studies. *Neuroimage* **155**, 394–405 (2017).
30. VA Kalatsky, MP Stryker, New paradigm for optical imaging: temporally encoded maps of intrinsic signal. *Neuron* **38**, 529–545 (2003).
31. Y Kamitani, F Tong, Decoding the visual and subjective contents of the human brain. *Nat. neuroscience* **8**, 679–685 (2005).
32. JD Haynes, G Rees, Predicting the orientation of invisible stimuli from activity in human primary visual cortex. *Nat. neuroscience* **8**, 686–691 (2005).
33. Y Kamitani, F Tong, Decoding seen and attended motion directions from activity in the human visual cortex. *Curr. biology* **16**, 1096–1102 (2006).
34. SA Harrison, F Tong, Decoding reveals the contents of visual working memory in early visual areas. *Nature* **458**, 632–635 (2009).
35. AM Albers, P Kok, I Toni, HC Dijkerman, FP De Lange, Shared representations for working memory and mental imagery in early visual cortex. *Curr. Biol.* **23**, 1427–1431 (2013).
36. Y Xing, T Ledgeway, PV McGraw, D Schluppeck, Decoding working memory of stimulus contrast in early visual cortex. *J. Neurosci.* **33**, 10301–10311 (2013).
37. L Reddy, N Tsuchiya, T Serre, Reading the mind's eye: decoding category information during mental imagery. *Neuroimage* **50**, 818–825 (2010).
38. RM Cichy, J Heinzle, JD Haynes, Imagery and perception share cortical representations of content and location. *Cereb. cortex* **22**, 372–380 (2012).
39. M Stokes, R Thompson, R Cusack, J Duncan, Top-down activation of shape-specific population codes in visual cortex during mental imagery. *J. Neurosci.* **29**, 1565–1572 (2009).
40. MR Johnson, MK Johnson, Decoding individual natural scene representations during perception and imagery. *Front. human neuroscience* **8**, 59 (2014).
41. J Erb, LM Schmitt, J Obleser, Temporal selectivity declines in the aging human auditory cortex. *Elife* **9**, e55300 (2020).
42. JV Haxby, et al., Distributed and overlapping representations of faces and objects in ventral temporal cortex. *Science* **293**, 2425–2430 (2001).
43. NP Issa, C Trepel, MP Stryker, Spatial frequency maps in cat visual cortex. *J. Neurosci.* **20**, 8504–8514 (2000).
44. HX Wang, EP Merriam, J Freeman, DJ Heeger, Motion direction biases and decoding in human visual cortex. *J. Neurosci.* **34**, 12601–12615 (2014).
45. BM Van Kemenade, K Seymour, TB Christophel, M Rothkirch, P Sterzer, Decoding pattern motion information in v1. *cortex* **57**, 177–187 (2014).
46. NV Swindale, A Grinvald, A Shmuel, The spatial pattern of response magnitude and selectivity for orientation and direction in cat visual cortex. *Cereb. cortex* **13**, 225–238 (2003).
47. NV Swindale, D Shoham, A Grinvald, T Bonhoeffer, M Hübener, Visual cortex maps are optimized for uniform coverage. *Nat. neuroscience* **3**, 822–826 (2000).
48. M Hübener, D Shoham, A Grinvald, T Bonhoeffer, Spatial relationships among three columnar systems in cat area 17. *J. Neurosci.* **17**, 9270–9284 (1997).
49. H Yu, BJ Farley, DZ Jin, M Sur, The coordinated mapping of visual space and response features in visual cortex. *Neuron* **47**, 267–280 (2005).
50. I Nauhaus, KJ Nielsen, AA Disney, EM Callaway, Orthogonal micro-organization of orientation and spatial frequency in primate primary visual cortex. *Nat. neuroscience* **15**, 1683–1690 (2012).
51. JC Horton, DL Adams, The cortical column: a structure without a function. *Philos. Transactions Royal Soc. B: Biol. Sci.* **360**, 837–862 (2005).
52. DL Adams, JC Horton, Monocular cells without ocular dominance columns. *J. neurophysiology* **96**, 2253–2264 (2006).
53. SV Girman, Y Sauvé', RD Lund, Receptive field properties of single neurons in rat primary visual cortex. *J. neurophysiology* **82**, 301–311 (1999).
54. EH Murphy, N Berman, The rabbit and the cat: a comparison of some features of response properties of single cells in the primary visual cortex. *J. Comp. Neurol.* **188**, 401–427 (1979).
55. SD Van Hooser, JAF Heimel, S Chung, SB Nelson, LJ Toth, Orientation selectivity without orientation maps in visual cortex of a highly visual mammal. *J. Neurosci.* **25**, 19–28 (2005).
56. KD Miller, Understanding layer 4 of the cortical circuit: a model based on cat v1. *Cereb. cortex* **13**, 73–82 (2003).
57. KD Miller, Canonical computations of cerebral cortex. *Curr. opinion neurobiology* **37**, 75–84 (2016).
58. D Ferster, KD Miller, Neural mechanisms of orientation selectivity in the visual cortex. *Annu. review neuroscience* **23**, 441–471 (2000).
59. M Kaschube, M Schnabel, F Wolf, Self-organization and the selection of pinwheel density in visual cortical development. *New journal physics* **10**, 015009 (2008).
60. L Chariker, R Shapley, M Hawken, LS Young, A theory of direction selectivity for macaque primary visual cortex. *Proc. Natl. Acad. Sci.* **118**, e2105062118 (2021).
61. J Antolík, et al., A comprehensive data-driven model of cat primary visual cortex. *PLOS Comput. Biol.* **20**, e1012342 (2024).
62. R Ben-Yishai, RL Bar-Or, H Sompolinsky, Theory of orientation tuning in visual cortex. *Proc. Natl. Acad. Sci.* **92**, 3844–3848 (1995).
63. AF Teich, N Qian, Comparison among some models of orientation selectivity. *J. neurophysiology* **96**, 404–419 (2006).
64. BA Olshausen, DJ Field, Emergence of simple-cell receptive field properties by learning a sparse code for natural images. *Nature* **381**, 607–609 (1996).
65. Y LeCun, Learning invariant feature hierarchies in *Computer Vision–ECCV 2012. Workshops and Demonstrations: Florence, Italy, October 7-13, 2012, Proceedings, Part I 12*. (Springer), pp. 496–505 (2012).

66. K Gregor, Y LeCun, Emergence of complex-like cells in a temporal product network with local receptive fields. *arXiv preprint arXiv:1006.0448* (2010).
67. J Antolik, JA Bednar, Development of maps of simple and complex cells in the primary visual cortex. *Front. computational neuroscience* **5**, 17 (2011).
68. M Zhu, CJ Rozell, Visual nonclassical receptive field effects emerge from sparse coding in a dynamical system. *PLoS computational biology* **9**, e1003191 (2013).
69. J Petitot, *Neurogéométrie de la vision*. (Springer), (2017).
70. N Montobbio, A Sarti, G Citti, A metric model for the functional architecture of the visual cortex. *SIAM J. on Appl. Math.* **80**, 1057–1081 (2020).
71. G Citti, A Sarti, From functional architectures to percepts: a neuromathematical approach in *Neuromathematics of Vision*. (Springer), pp. 131–171 (2014).
72. Y Li, D Fitzpatrick, LE White, The development of direction selectivity in ferret visual cortex requires early visual experience. *Nat. neuroscience* **9**, 676–681 (2006).
73. Y Li, SD Van Hooser, M Mazurek, LE White, D Fitzpatrick, Experience with moving visual stimuli drives the early development of cortical direction selectivity. *Nature* **456**, 952–956 (2008).
74. T Yokoo, B Knight, L Sirovich, An optimization approach to signal extraction from noisy multivariate data. *Neuroimage* **14**, 1309–1326 (2001).
75. J Ribot, S Tanaka, H Tanaka, A Ajima, Online analysis method for intrinsic signal optical imaging. *J. neuroscience methods* **153**, 8–20 (2006).